Pressure-induced superconductivity in the Zintl topological insulator $SrIn_2As_2$

Weizheng Cao,[1,*] Haifeng Yang,[1,2,*] Yongkai Li,[3,4,*] Cuiying Pei,[1] Qi Wang,[1,2] Yi Zhao,[1] Changhua Li,[1] Mingxin Zhang,[1] Shihao Zhu,[1] Juefei Wu,[1] Lili Zhang,[5] Zhiwei Wang,[3,4,†] Yugui Yao,[3] Zhongkai Liu,[1,2,‡] Yulin Chen,[1,2,6] and Yanpeng Qi[1,2,7,§]

[1]*School of Physical Science and Technology, ShanghaiTech University, Shanghai 201210, China*
[2]*ShanghaiTech Laboratory for Topological Physics, ShanghaiTech University, Shanghai 201210, China*
[3]*Centre for Quantum Physics, Key Laboratory of Advanced Optoelectronic Quantum Architecture and Measurement (MOE), School of Physics, and Beijing Key Lab of Nanophotonics and Ultrafine Optoelectronic Systems, Beijing Institute of Technology, Beijing 100081, China*
[4]*Material Science Center, Yangtze Delta Region Academy of Beijing Institute of Technology, Jiaxing, 314011, China*
[5]*Shanghai Synchrotron Radiation Facility, Shanghai Advanced Research Institute, Chinese Academy of Sciences, Shanghai 201203, China*
[6]*Department of Physics, Clarendon Laboratory, University of Oxford, Parks Road, Oxford OX1 3PU, United Kingdom*
[7]*Shanghai Key Laboratory of High-Resolution Electron Microscopy, ShanghaiTech University, Shanghai 201210, China*

(Received 29 July 2023; accepted 14 November 2023; published 15 December 2023)

The Zintl compound AIn_2X_2 (A = Ca, Sr, and X = P, As), as a theoretically predicted nonmagnetic topological insulator, requires experiments to understand its electronic structure and topological characteristics. In this paper, we systematically investigate the crystal structures and electronic properties of the Zintl compound $SrIn_2As_2$ under both ambient and high-pressure conditions. By means of angle-resolved photoemission spectroscopy, we observe the overall band structures and "tails" of the topological surface states on the (001) surface that qualitatively agree well with *ab initio* calculations, thus suggesting $SrIn_2As_2$ as a topological insulator. Interestingly, application of pressure effectively tunes the crystal structure and electronic properties of $SrIn_2As_2$. Superconductivity is observed in $SrIn_2As_2$ for pressure where the temperature dependence of the resistivity changes from a semiconductinglike behavior to that of a metal. The observation of nontrivial topological states and pressure-induced superconductivity in $SrIn_2As_2$ provides crucial insights into the relationship between topology and superconductivity, and also stimulates further studies of superconductivity in topological materials.

DOI: 10.1103/PhysRevB.108.224510

I. INTRODUCTION

Topological insulators (TIs) are a novel class of materials that possess both gapped bulk and exotic metallic surface states. The robust topological surface state (TSS) in TIs has been confirmed by angle-resolved photoemission spectroscopy (ARPES) [1,2] and scanning tunneling microscopy (STM) [3–5], and has also been characterized by magnetotransport such as Shubnikov–de Haas (SdH) oscillation [6,7], etc. Due to the dissipationless flow of electric current at the surface, TIs have been projected as promising candidates for developing next-generation, low power consuming, high-speed electronic, optoelectronic, and spintronic devices. The interplay between symmetry and topology in crystalline solids leads to other emerging topological quantum materials (TQMs), including topological crystalline insulators [8–11], higher-order topological insulators [12,13], Dirac [14,15], Weyl [2,16–18], nodal line [19,20], and multifold semimetals [21,22].

Since they were first discovered by Zintl in the early 1900s [23], Zintl compounds have been extensively studied for their fascinating physical properties, including superconductivity, colossal magnetoresistance, magnetic order, mixed valence, thermoelectricity, and so on [24–30]. Several Zintl compounds have recently garnered attention due to their interesting topological properties. For instance, $EuIn_2As_2$ exhibits A-type antiferromagnetic (AFM) ordering at $T_N \sim 16$ K [31], and is predicted to be a promising candidate for axion topological insulators [32]. ARPES results indicated a hole-type Fermi pocket around the Brillouin zone and the AFM transition accompanied by the axion insulator phase [33,34]. The magnetotransport characterization revealed an anomalous Hall effect (AHE) originating from a nonvanishing Berry curvature and a large topological Hall effect (THE), which is attributed to the scalar spin chirality of the noncoplanar spin structure caused by the external field [35]. Another Zintl compound, $SrIn_2As_2$, which is isostructural with $EuIn_2As_2$, has been predicted to be a dual topological insulator with nontrivial $Z_2 = 1$ and mirror Chern number $C_M = -1$ via first-principles calculations together with symmetry analysis [36]. Furthermore, the AIn_2X_2 (A = Ca, Sr, and X = P, As) family exhibits a narrow band gap which can be easily tuned by high pressure or chemical doping [37–40]. Theoretical calculations indicated that the pressure-induced band gap decreases to zero at 6.6 GPa and then reopens, and $SrIn_2As_2$

*These authors contributed equally to this work.
†zhiweiwang@bit.edu.cn
‡liuzhk@shanghaitech.edu.cn
§qiyp@shanghaitech.edu.cn

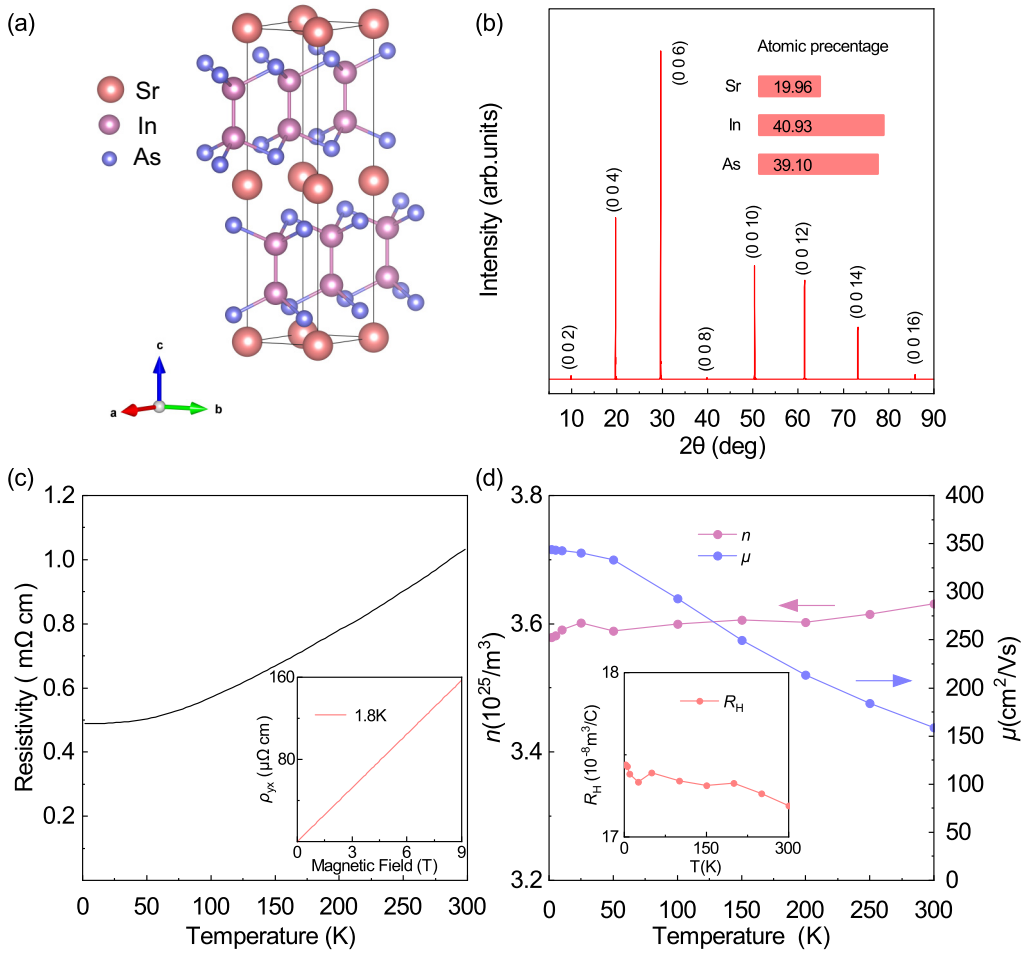

FIG. 1. (a) The crystal structure of $SrIn_2As_2$ with a space group $P6_3/mmc$. (b) The room-temperature x-ray diffraction peaks from the *ab* plane of $SrIn_2As_2$ single crystal. Inset: the elemental content of $SrIn_2As_2$. (c) Resistivity of the $SrIn_2As_2$ single crystal from 1.8 to 300 K. Inset: Hall resistivity [$\rho_{yx}(H)$] as a function of magnetic field at 1.8 K with magnetic field applied along the *c*-axis direction: (d) Carrier density *n* and mobility μ of $SrIn_2As_2$ as a function of temperature. Inset: temperature dependence of Hall coefficient R_H for $SrIn_2As_2$.

exhibits a gapless nontrivial topological surface state, indicating a strong topological insulator [41]. However, these theoretical predictions have not been experimentally verified yet, and further investigation of the evolution of the physical properties of AIn_2X_2 under pressure is required.

In this work, we choose the Zintl compound $SrIn_2As_2$, one member of the AIn_2X_2 family, to systematically investigate the crystal structures and electronic properties under both ambient and high-pressure conditions. The transport measurements reveal metallic behavior for $SrIn_2As_2$ with hole-dominated carriers. ARPES results reveal the "tails" of topological Dirac surface states on the (001) surface, which is consistent with previous theoretical calculation [36]. Interestingly, superconductivity was observed at around 30 GPa and persisted at approximately 2.1 K until the maximum experimental pressure. The pressure-induced structure phase transition in the Zintl compound $SrIn_2As_2$ is also discussed.

II. EXPERIMENTAL DETAILS

The single crystals of $SrIn_2As_2$ were grown by the self-flux method. High-purity starting materials of Sr, In, and As were loaded in a quartz tube with the ratio of Sr : In : As = 1 : 12 : 2. The tube was sealed after it was evacuated to a vacuum of 2×10^{-4} Pa. The raw materials were reacted and homogenized at 1373 K for several hours, followed by cooling down to 873 K at a rate of 2 K/h. Finally, a shiny crystal with an apparent hexagonal edge was obtained after the indium flux was removed by centrifuge. The crystalline phase of $SrIn_2As_2$ was checked by single-crystalline x-ray diffraction (XRD, Cu $K\alpha$, $\lambda = 1.54184$ Å). The chemical composition value of $SrIn_2As_2$ was given by energy-dispersive x-ray spectra (EDX). Transmission electron microscopy (TEM) measurements were carried out on a $SrIn_2As_2$ sample after being high pressure treated at 61.5 GPa. Electrical transport properties including resistivity, magnetoresistance, and Hall effect were performed on a physical property measurement system (PPMS).

In order to investigate the band structures of $SrIn_2As_2$, we performed systematic synchrotron-based ARPES measurements at BL03U of the Shanghai Synchrotron Radiation Facility. Data were recorded by a Scienta Omicron DA30L analyzer. The measurement sample temperature and pressure were 15 K and 7×10^{-11} mbar, respectively. The overall energy and angle resolutions were ~ 10 meV and 0.2°, respectively. Fresh (001) surfaces were obtained for

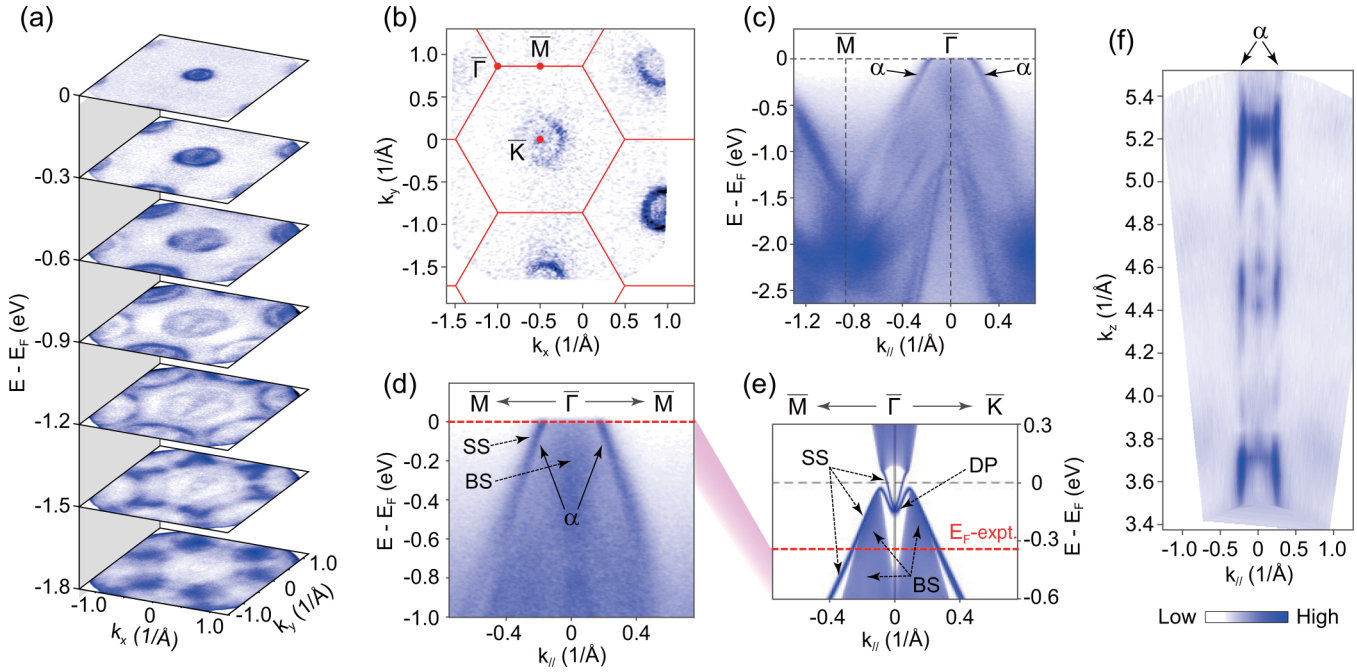

FIG. 2. ARPES measurements on $SrIn_2As_2$ crystals. (a) Stacking plot of constant-energy contours measured in 98 eV photons with linearly horizontal polarization. (b) Fermi surface map across multiple Brillouin zones measured using 110 eV photons. The red lines represent the projected Brillouin zone. (c) High-symmetry band dispersion along the $\bar{\Gamma} - \bar{M}$ direction. (d) Close-up of the $\bar{\Gamma} - \bar{M}$ dispersion near the Fermi level. BS/SS is short for bulk/surface states. (e) Calculated $\bar{\Gamma} - \bar{M}$ dispersion clearly shows the Dirac surface states, reproduced from Ref. [36]. DP is short for Dirac point. The dotted red line qualitatively marks the Fermi level from the ARPES measurements. (f) Photon energy dependent measurements apparently confirm the surface state nature of the α bands. The photon energy used ranges from 40 to 110 eV.

measurements by *in situ* cleaving the crystals at low temperatures. No signatures of the surface aging were observed during measurements.

High-pressure electrical transport measurements were performed in a nonmagnetic diamond anvil cell (DAC) [42–45]. A cubic BN/epoxy mixture layer was inserted between BeCu gaskets and electrical leads. Four platinum sheet electrodes were touched to the sample for resistance measurements with the van der Pauw method. Pressure was determined by the ruby luminescence method [46]. An *in situ* high-pressure Raman spectroscopy investigation was performed using a Raman spectrometer (Renishaw inVia, UK) with a laser excitation wavelength of 532 nm and a low wave number filter. A symmetric DAC with anvil culet sizes of 200 μm was used, with silicon oil as pressure transmitting medium (PTM). *In situ* high-pressure XRD measurements were performed at beamline BL15U of the Shanghai Synchrotron Radiation Facility (x-ray wavelength $\lambda = 0.6199$ Å). A symmetric DAC with anvil culet sizes of 200 μm and Re gaskets were used. Silicon oil was used as the PTM and pressure was determined by the ruby luminescence method [46]. The two-dimensional diffraction images were analyzed using FIT2D software [47]. Rietveld refinements of crystal structure under various pressures were performed using GSAS and the graphical user interface EXPGUI [48,49].

III. RESULTS AND DISCUSISION

Figure 1(a) shows the crystal structure of $SrIn_2As_2$, which adopts a hexagonal structure with a space group $P6_3/mmc$. The In and As atoms form two layers of a two-dimensional zigzag honeycomb lattice with mirror symmetry, forming $[In_2As_2]^{2-}$ polyanions through staggered stacking. Layers of Sr^{2+} and $[In_2As_2]^{2-}$ are alternately stacked along the [0 0 1] direction. The single-crystal XRD pattern of $SrIn_2As_2$ displays sharp [0 0 l] diffraction peaks [Figure 1(b)]. The extracted lattice parameter is $c = 18.08$ Å, which is consistent with a previous report [37]. Chemical composition analysis from EDX measurement on the single crystal reveals good stoichiometry with an atomic percentage of Sr : In : As = 19.96 : 40.93 : 39.10, as shown in the inset of Fig. 1(b). These characterizations indicate the high quality of our samples.

Next, we carried out transport measurements at ambient pressure. Figure 1(c) shows the temperature dependence of resistivity for $SrIn_2As_2$, which reveals metallic behavior with residual resistivity ratio (RRR)= 2.11. The longitudinal resistivity (ρ_{xx}) and Hall resistivity (ρ_{yx}) were measured with the magnetic field applied along the c axis at various temperatures ranging from 1.8 to 300 K, as shown in Fig. S1 in the Supplemental Material [50]. The positive magnetoresistance is observed in all the temperature range and reaches ~0.47% at 1.8 K and 9 T. At 1.8 K, ρ_{yx} displays a linear dependence on the magnetic field with a positive slope, indicating that the hole carriers play a dominant role in the transport. This is also consistent with our ARPES measurements shown below. However, ρ_{yx} shows almost temperature independent behavior with a rather slight change over the measured temperature range. Hall resistivity is fitted using a single-band model, i.e., $\rho_{yx} = R_H B$, where $R_H = 1/en$ is the Hall coefficient. Figure 1(d) shows the temperature dependence of carrier

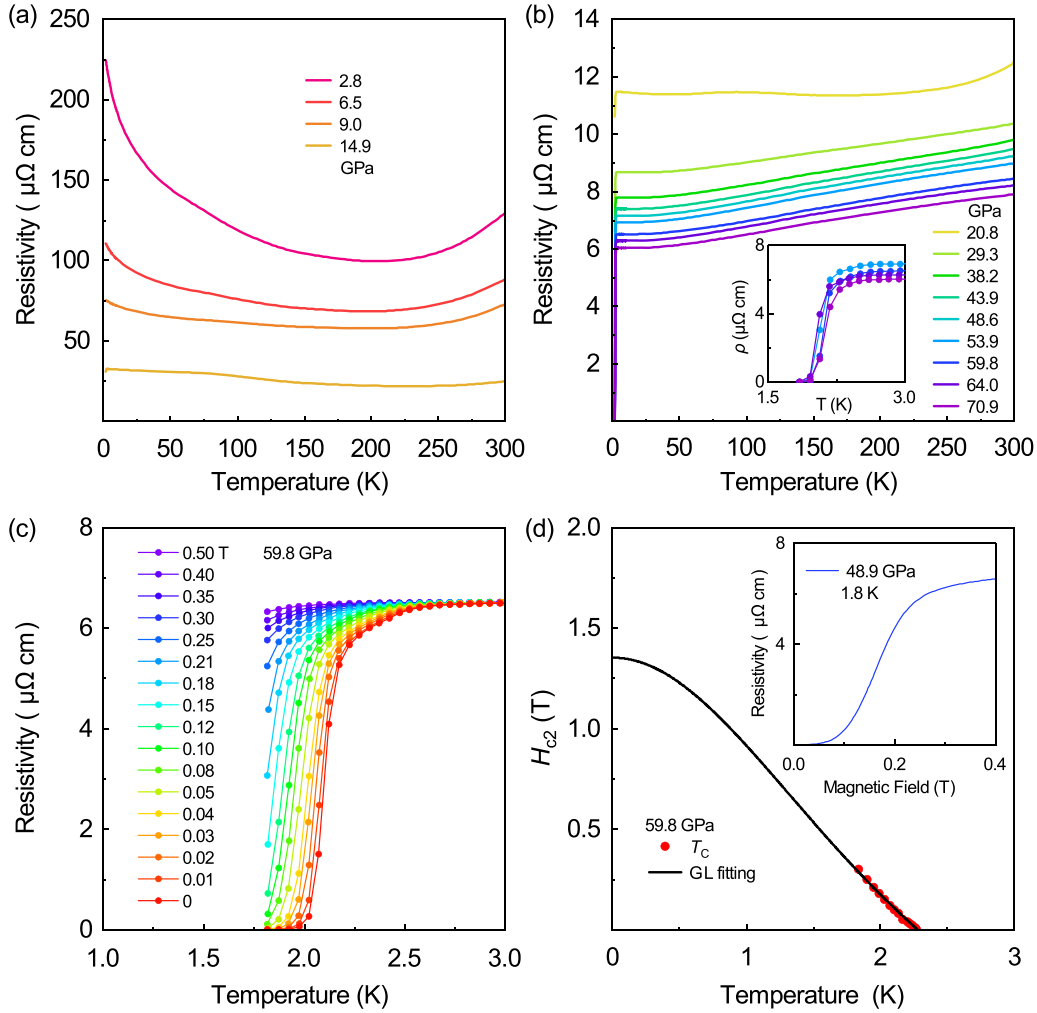

FIG. 3. Transport properties of $SrIn_2As_2$ as a function of pressure. (a) Electrical resistivity of $SrIn_2As_2$ as a function of temperature from 2.9 to 14.9 GPa in run III. (b) Electrical resistivity of $SrIn_2As_2$ as a function of temperature from 20.8 to 70.9 GPa in run III. Inset: Temperature-dependent resistivity of $SrIn_2As_2$ in the vicinity of the superconducting transition. (c) Resistivity as a function of temperature at a pressure of 59.8 GPa under different magnetic fields for $SrIn_2As_2$ in run III. (d) Temperature dependence of upper critical field for $SrIn_2As_2$ at 59.8 GPa. T_c is determined as the 90% drop of the normal state resistivity. The solid lines represent the Ginzburg-Landau (GL) fitting. The $\mu_0 H_{c2}(0)$ is 1.35 T. Inset: Resistivity as a function of magnetic field at 1.8 K. The superconductivity state is suppressed for field sufficiently away from 0.4 T.

density n and carrier mobility μ. The carrier density n reaches 3.58×10^{25} m^{-3} and carrier mobility μ is estimated to be 343.94 cm^2 V^{-1} s^{-1} at 1.8 K, which is comparable with other topological materials [51].

Figures 2(a) and 2(b) display the measured constant-energy contours of $SrIn_2As_2$. The Fermi surface of $SrIn_2As_2$ is mainly composed of a circle encircling the $\bar{\Gamma}$ point. Inside the circle, some blurry features are also discernible. When going toward high binding energy regions, the circle keeps expanding, and circles from other adjacent Brillouin zones connect with each other to form a hexagon, consistent with the crystal symmetry of the (001) surface. If cutting the Fermi surface along the $\bar{\Gamma} - \bar{M}$ direction, one can see the sharp holelike band dispersion marked as α that contributes to the circle Fermi surface, and multiple blurry bands residing between the two α bands [Figs. 2(c) and 2(d)]. These dispersions exhibit qualitative agreement with previous theoretical calculations proposing $SrIn_2As_2$ is a dual topological insulator and hosts topological Dirac surface states on the (001) surface [Fig. 2(e)] [36]. However, we have not observed the whole Dirac surface state dispersion (including the Dirac point) as the crystals appear to be heavily p doped compared to the calculations [the red dotted line is the Fermi level from experiments in Fig. 2(e)]. We tried *in situ* potassium doping but the shift-up of the Fermi level is quite limited. We ascribe the observed α bands to be the tail of the Dirac surface states. Their surface state nature is further verified by the detailed photon-energy dependence measurements as they show negligible k_z dispersions [Fig. 2(f)].

The Zintl compound $SrIn_2As_2$ with a narrow band gap is extremely sensitive to external pressure. In addition, first-principles calculations indicate that $SrIn_2As_2$ will undergo insulator-metal phase transition and topological quantum phase transition under pressure modulation. Indeed, the high-pressure approach has been widely employed in recent studies of topological materials and has led to many interesting

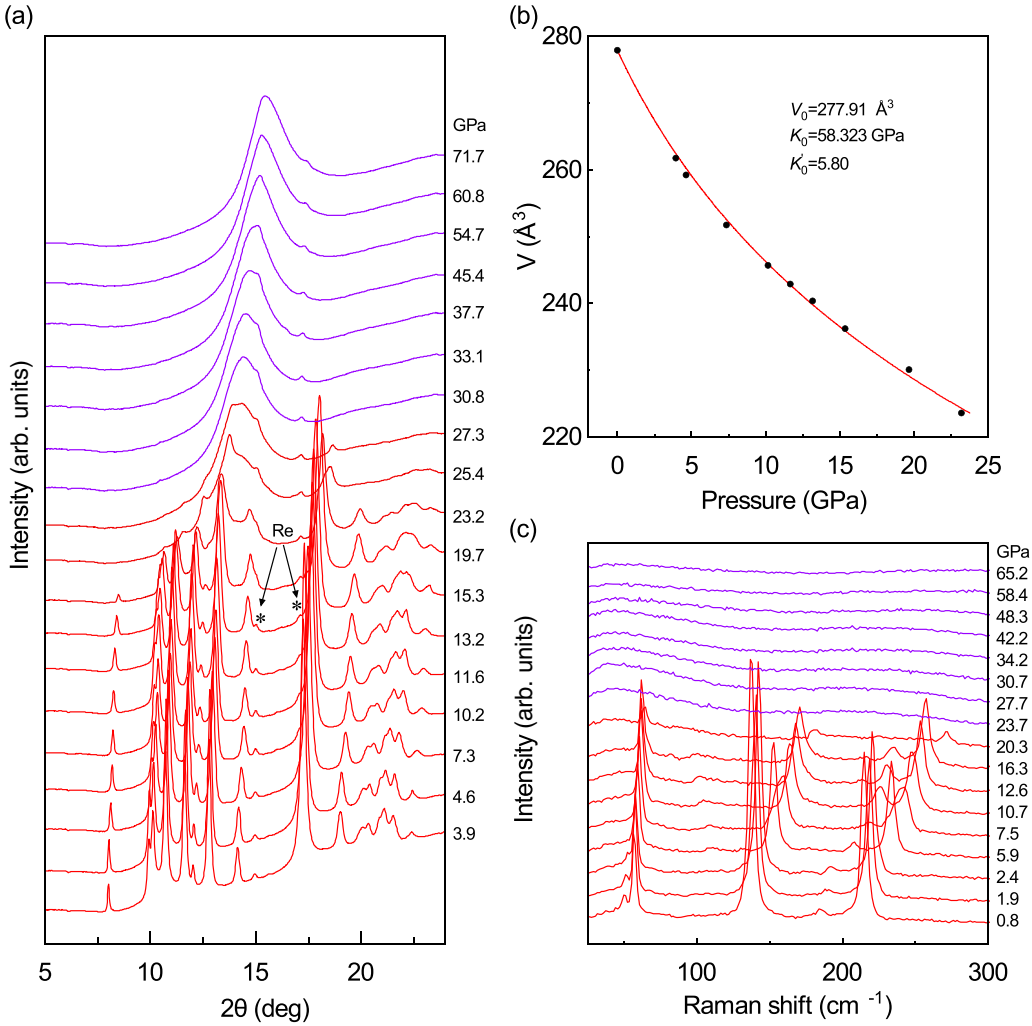

FIG. 4. (a) XRD patterns of $SrIn_2As_2$ under different pressures up to 71.7 GPa. (b) Variation in unit cell volume of $SrIn_2As_2$ with pressure at 300 K. Black circles: experiments. Solid lines are third-order Birch-Murnaghan fits to the data. The third-order Birch-Murnaghan equation of state (EOS) is given by $P = \frac{3}{2}K_0[(\frac{V_0}{V})^{\frac{7}{3}} - (\frac{V_0}{V})^{\frac{5}{3}}]\{1 + \frac{3}{4}(K_0' - 4)[(\frac{V_0}{V})^{\frac{2}{3}} - 1]\}$. (c) Raman spectra of $SrIn_2As_2$ under pressure at room temperature.

results [52–54]. Hence, we are motivated to investigate the effect of high pressure on the electrical transport properties of $SrIn_2As_2$. Figure 3 shows temperature dependence of the electrical resistivity $\rho(T)$ of $SrIn_2As_2$ for pressure up to 70.9 GPa. At the low-pressure region, the $\rho(T)$ first decreases with decreasing temperature and reaches a minimum value. Then the $\rho(T)$ gradually increases showing semiconductinglike behavior at 2.8 GPa with a negative $d\rho/dT$ slope [Fig. 3(a)]. The anomalous $\rho(T)$ of $SrIn_2As_2$ implies that the carriers are weakly localized at low temperature due to strong quantum coherence [40]. Upon further increasing the pressure, the resistivity at 300 K begins to decrease rapidly and the semiconductinglike behavior is suppressed, accompanied by a drop of $\rho(T)$ at the lowest temperature ($T_{min} = 1.8$ K), as shown in the inset of Fig. 3(a). With pressure increasing, the drop of $\rho(T)$ becomes more pronounced and zero resistivity is achieved at low temperature for $P > 53.9$ GPa, indicating the emergence of a superconducting transition. Moreover, the superconductivity with $T_c \sim 2.1$ K is robust and persists until the maximum pressure of 70.9 GPa [Fig. 3(b)].

To gain insights into the superconducting transition, we applied an external magnetic field on $SrIn_2As_2$ at 48.9 and 59.8 GPa. It is clear that the magnetic field could suppress superconducting transition [inset of Fig. 3(d)]. T_c gradually shifts toward lower temperatures with the increase of the magnetic field. A magnetic field $\mu_0 H = 0.5$ T removes all signs of superconductivity above 1.8 K as shown in Fig. 3(c). These results further confirm pressure-induced bulk superconductivity in $SrIn_2As_2$. The derived upper critical field $\mu_0 H_{c2}$ as a function of temperature can be well fitted using the empirical Ginzburg-Landau formula $\mu_0 H_{c2}(T) = \mu_0 H_{c2}(T)(1 - t^2)/(1 + t^2)$, where $t = T/T_c$ is the reduced temperature with zero-field superconducting T_c. The extrapolated upper critical field $\mu_0 H_{c2}(0)$ of $SrIn_2As_2$ from the 90% ρ_n criterion can reach 1.35 T at 59.8 GPa, which yields a Ginzburg-Landau coherence length $\xi_{GL}(0)$ of 15.60 nm. It is worth noting that the value of $\mu_0 H_{c2}(0)$ is well below the Pauli-Clogston limit.

To further identify the origin of superconductivity in $SrIn_2As_2$, *in situ* x-ray diffraction (XRD) measurements have

been carried out to analyze the structure evolution under various pressures. Figure 4(a) shows the high-pressure synchrotron XRD patterns measured at room temperature up to 71.7 GPa. A representative refinement at 3.9 GPa is displayed in Fig. S3(a) [50]. At the lower-pressure region, all the diffraction peaks can be indexed well to the hexagonal structure with a space group $P6_3/mmc$. The small peaks marked with an asterisk represent the signal of the rhenium gasket. Further increase of the applied pressure gives rise to the shift of the Bragg peaks to larger angles, due to the lattice shrinkage, as shown in the pressure dependences of the lattice parameters in Fig. S3(b) [50]. The experiment pressure-volume (P-V) data can be well fitted using the third-order Birch-Murnaghan equation of state (EOS) [55], whose obtained bulk modulus K_0 is 58.32 GPa with $V_0 = 277.91$ Å^3 and $K_0' = 5.80$. The structure of $SrIn_2As_2$ is robust and there is no structural phase transition until 23.2 GPa. However, when the pressure increases up to 30.8GPa, a broad peak appears around 14.4 ° in the diffraction patterns, indicating the application of high pressure introduced amorphous phases in the $SrIn_2As_2$. A similar phenomenon was observed in some other materials [52,54,56–61]. It should be mentioned that the superconductivity is observed where pressure increases up to 30 GPa. In addition, we did not observe other peaks from other elements (e.g., Sr, In, or As) [62–65]; the possibility of high-pressure decomposition of $SrIn_2As_2$ is hence ruled out. To derive more structural information, high-pressure *in situ* Raman spectroscopy measurements were carried out. As shown in Fig. 4(c), Raman active modes are clearly observed at the lower-pressure regions. With increasing pressure, the profile of the spectra remains similar to that at lower pressure, whereas the observed modes exhibit blueshift, thus showing the normal pressure behavior. An abrupt disappearance of Raman peaks for pressure near 23.7 GPa indicates the structural phase transition to an amorphous phase. The evolution of the Raman spectra is consistent with our synchrotron XRD patterns.

Several independent high-pressure transport measurements on $SrIn_2As_2$ single crystals provide consistent and reproducible results, confirming intrinsic superconductivity under high pressure. From resistivity, XRD, and Raman measurements, we can construct a T-P phase diagram of $SrIn_2As_2$ (Fig. 5). In the lower-pressure region, the $\rho(T)$ decreases upon cooling in a metallic manner first and then attains a minimum value. Subsequently, the $\rho(T)$ upturns rapidly just like a semiconductor characteristic. Such anomalous $\rho(T)$ behavior due to weak localization effect provides a signal of quantum correction to conductance in $SrIn_2As_2$ [40]. Upon further increasing the pressure, the resistivity at room temperature as well as 3 K begins to drop rapidly and the semiconductorlike behavior is suppressed. Superconductivity is observed after the temperature dependence of $\rho(T)$ changes from a semiconductinglike behavior to that of a metal. The T_c of $SrIn_2As_2$ rises to 2.1 K and persists until the maximum pressure of this work. Above 30 GPa, *in situ* high-pressure XRD demonstrated that a pressure-induced amorphization emerges. The high-pressure amorphous phase of $SrIn_2As_2$ is retained after the pressure is released, which is confirmed by TEM measurements (Figs. S3(c) and S3(d) [50]). It is very interesting that an amorphous phase of $SrIn_2As_2$ could support superconductivity. This will be a stimulus for further research from an experimental and theoretical point of view.

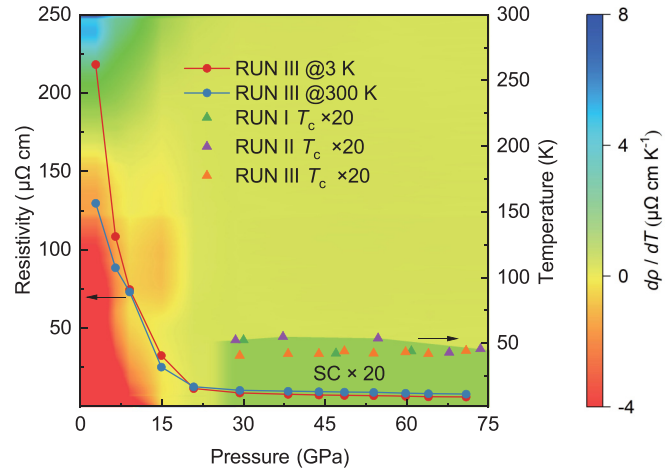

FIG. 5. Phase diagram of $SrIn_2As_2$. The red and blue dotted line plots depict the resistivity as a function of temperature at 3 and 300 K, respectively. The left vertical axis represents the resistivity at 3 and 300 K. Superconductivity with $T_c \sim 2.1$ K is observed as the pressure increases from around 21 GPa until the maximum pressure. The green, purple, and orange triangles represent the T_c in different experimental runs, respectively. The right vertical axis represents the superconducting transition temperature. The background depicts the dependence of dρ/dT on temperature at various pressure levels.

IV. CONCLUSION

In summary, we have successfully grown high-quality single crystals of the Zintl compound $SrIn_2As_2$. Combining the transports and ARPES measurements, we indicate that $SrIn_2As_2$ is a strong topological insulator. Moreover, we discovered pressure-induced superconductivity in $SrIn_2As_2$, and T_c still persists until a maximum experimental pressure. Our results demonstrate that the nontrivial topological state and the pressure-induced superconductivity were all observed in $SrIn_2As_2$. Thus, the Zintl AIn_2X_2 (A = Ca, Sr, and X = P, As) family provides an excellent platform for further understanding the relationship between the topological phase and superconductivity.

ACKNOWLEDGMENTS

This work was supported by the National Natural Science Foundation of China (Grants No. 52272265, No. U1932217, No. 11974246, and No. 12004252), the National Key R&D Program of China (Grant No. 2018YFA0704300), and Shanghai Science and Technology Plan (Grant No. 21DZ2260400). H.Y. acknowledges the support from the Shanghai Sailing Program (Grant No. 20YF1430500) and the National Natural Science Foundation of China (Grant No. 12004248). Z. L. acknowledges the support from the National Natural Science Foundation of China (Grant No. 12274298) and the National Key R&D program of China (Grant No. 2022YFA1604400/03). Z.W. acknowledges the support from the National Key R&D Program of China (Grants No.

2020YFA0308800 and No. 2022YFA1403400), the Natural Science Foundation of China (Grant No. 92065109), and the Beijing Natural Science Foundation (Grants No. Z210006 and No. Z190006). The authors acknowledge the Analytical Instrumentation Center (Grant No. SPST-AIC10112914), SPST, ShanghaiTech University and the Analysis and Testing Center at Beijing Institute of Technology for assistance in facility support. The authors thank the staff at BL15U1 at Shanghai Synchrotron Radiation Facility for assistance during data collection.

[1] B. Lv, N. Xu, H. Weng, J. Ma, P. Richard, X. Huang, L. Zhao, G. Chen, C. Matt, and F. Bisti, Observation of Weyl nodes in TaAs, Nat. Phys. **11**, 724 (2015).

[2] S. Y. Xu, I. Belopolski, N. Alidoust, M. Neupane, G. Bian, C. Zhang, R. Sankar, G. Chang, Z. Yuan, and C.-C. Lee, Discovery of a Weyl fermion semimetal and topological Fermi arcs, Science **349**, 613 (2015).

[3] C. L. Song, Y. P. Jiang, Y. L. Wang, Z. Li, L. Wang, K. He, X. Chen, X. C. Ma, and Q. K. Xue, Gating the charge state of single Fe dopants in the topological insulator Bi_2Se_3 with a scanning tunneling microscope, Phys. Rev. B **86**, 045441 (2012).

[4] M. Chen, J.-P. Peng, H. M. Zhang, L. L. Wang, K. He, X. C. Ma, and Q. K. Xue, Molecular beam epitaxy of bilayer Bi (111) films on topological insulator Bi_2Te_3: A scanning tunneling microscopy study, Appl. Phys. Lett. **101**, 081603 (2012).

[5] X. B. Li, W. K. Huang, Y.-Y. Lv, K. W. Zhang, C. L. Yang, B. B. Zhang, Y. Chen, S. H. Yao, J. Zhou, and M. H. Lu, Experimental observation of topological edge states at the surface step edge of the topological insulator $ZrTe_5$, Phys. Rev. Lett. **116**, 176803 (2016).

[6] G. Eguchi, K. Kuroda, K. Shirai, A. Kimura, and M. Shiraishi, Surface Shubnikov–de Haas oscillations and nonzero Berry phases of the topological hole conduction in $Tl_{1-x}Bi_{1+x}Se_2$, Phys. Rev. B **90**, 201307(R) (2014).

[7] L. Fang, Y. Jia, D. Miller, M. Latimer, Z. Xiao, U. Welp, G. Crabtree, and W. K. Kwok, Catalyst-free growth of millimeter-long topological insulator Bi_2Se_3 nanoribbons and the observation of the π-Berry phase, Nano Lett. **12**, 6164 (2012).

[8] L. Fu, Topological crystalline insulators, Phys. Rev. Lett. **106**, 106802 (2011).

[9] T. H. Hsieh, H. Lin, J. Liu, W. Duan, A. Bansil, and L. Fu, Topological crystalline insulators in the SnTe material class, Nat. Commun. **3**, 982 (2012).

[10] J. Kruthoff, J. De Boer, J. Van Wezel, C. L. Kane, and R.-J. Slager, Topological classification of crystalline insulators through band structure combinatorics, Phys. Rev. X **7**, 041069 (2017).

[11] R.-J. Slager, A. Mesaros, V. Juričić, and J. Zaanen, The space group classification of topological band-insulators, Nat. Phys. **9**, 98 (2013).

[12] F. Schindler, A. M. Cook, M. G. Vergniory, Z. Wang, S. S. Parkin, B. A. Bernevig, and T. Neupert, Higher-order topological insulators, Sci. Adv. **4**, eaat0346 (2018).

[13] F. Schindler, Z. Wang, M. G. Vergniory, A. M. Cook, A. Murani, S. Sengupta, A. Y. Kasumov, R. Deblock, S. Jeon, and I. Drozdov, Higher-order topology in bismuth, Nat. Phys. **14**, 918 (2018).

[14] Z. Liu, B. Zhou, Y. Zhang, Z. Wang, H. Weng, D. Prabhakaran, S. K. Mo, Z. Shen, Z. Fang, and X. Dai, Discovery of a three-dimensional topological Dirac semimetal, Na_3Bi, Science **343**, 864 (2014).

[15] Z. Liu, J. Jiang, B. Zhou, Z. Wang, Y. Zhang, H. Weng, D. Prabhakaran, S. K. Mo, H. Peng, and P. Dudin, A stable three-dimensional topological Dirac semimetal Cd_3As_2, Nat. Mater. **13**, 677 (2014).

[16] B. Lv, H. Weng, B. Fu, X. P. Wang, H. Miao, J. Ma, P. Richard, X. Huang, L. Zhao, and G. Chen, Experimental discovery of Weyl semimetal TaAs, Phys. Rev. X **5**, 031013 (2015).

[17] S. Y. Xu, N. Alidoust, G. Chang, H. Lu, B. Singh, I. Belopolski, D. S. Sanchez, X. Zhang, G. Bian, and H. Zheng, Discovery of Lorentz-violating type II Weyl fermions in LaAlGe, Sci. Adv. **3**, e1603266 (2017).

[18] W. Cao, Y. Su, Q. Wang, C. Pei, L. Gao, Y. Zhao, C. Li, N. Yu, J. Wang, and Z. Liu, Quantum oscillations in noncentrosymmetric Weyl semimetal SmAlSi, Chin. Phys. Lett. **39**, 047501 (2022).

[19] C. Fang, H. Weng, X. Dai, and Z. Fang, Topological nodal line semimetals, Chin. Phys. B **25**, 117106 (2016).

[20] C. Fang, Y. Chen, H.-Y. Kee, and L. Fu, Topological nodal line semimetals with and without spin-orbital coupling, Phys. Rev. B **92**, 081201(R) (2015).

[21] C. Le and Y. Sun, Topology and symmetry of circular photogalvanic effect in the chiral multifold semimetals: A review, J. Phys.: Condens. Matter **33**, 503003 (2021).

[22] Z. Ni, K. Wang, Y. Zhang, O. Pozo, B. Xu, X. Han, K. Manna, J. Paglione, C. Felser, and A. G. Grushin, Giant topological longitudinal circular photo-galvanic effect in the chiral multifold semimetal CoSi, Nat. Commun. **12**, 154 (2021).

[23] E. Zintl, Intermetallische verbindungen, Angew. Chem. **52**, 1 (1939).

[24] N. Varnava, T. Berry, T. M. McQueen, and D. Vanderbilt, Engineering magnetic topological insulators in $Eu_5M_2X_6$ Zintl compounds, Phys. Rev. B **105**, 235128 (2022).

[25] J. Wang, X. Cui, Y. Wan, T. Ying, S. Li, and J. Guo, Superconductivity in layered Zintl phase $LiSn_2As_2$, arXiv:2111.11319.

[26] J. Wang, T. Ying, J. Deng, C. Pei, T. Yu, X. Chen, Y. Wan, M. Yang, W. Dai, and D. Yang, Superconductivity in an orbital-reoriented SnAs square lattice: A case study of $Li_{0.6}Sn_2As_2$ and NaSnAs, Angew. Chem. **135**, e202216086 (2023).

[27] T. Qin, R. Zhong, W. Cao, S. Shen, C. Wen, Y. Qi, and S. Yan, Real-space observation of unidirectional charge density wave and complex structural modulation in the pnictide superconductor $Ba_{1-x}Sr_xNi_2As_2$, Nano Lett. **23**, 2958 (2023).

[28] Y. Qi, Z. Gao, L. Wang, D. Wang, X. Zhang, and Y. Ma, Superconductivity at 34.7 K in the iron arsenide $Eu_{0.7}Na_{0.3}Fe_2As_2$, New J. Phys. **10**, 123003 (2008).

[29] Z. Gao, Y. Qi, L. Wang, D. Wang, X. Zhang, C. Yao, C. Wang, and Y. Ma, Synthesis and properties of La-doped $CaFe_2As_2$ single crystals with $T_c = 42.7$ K, Europhys. Lett. **95**, 67002 (2011).

[30] Y. Qi, Z. Gao, L. Wang, D. Wang, X. Zhang, C. Yao, C. Wang, C. Wang, and Y. Ma, Transport properties and anisotropy in rare-earth doped $CaFe_2As_2$ single crystals with T_c above 40 K, Supercond. Sci. Technol. **25**, 045007 (2012).

[31] A. M. Goforth, P. Klavins, J. C. Fettinger, and S. M. Kauzlarich, Magnetic properties and negative colossal magnetoresistance of the rare earth Zintl phase $EuIn_2As_2$, Inorg. Chem. **47**, 11048 (2008).

[32] Y. Xu, Z. Song, Z. Wang, H. Weng, and X. Dai, Higher-order topology of the axion insulator $EuIn_2As_2$, Phys. Rev. Lett. **122**, 256402 (2019).

[33] S. Regmi, M. M. Hosen, B. Ghosh, B. Singh, G. Dhakal, C. Sims, B. Wang, F. Kabir, K. Dimitri, and Y. Liu, Temperature-dependent electronic structure in a higher-order topological insulator candidate $EuIn_2As_2$, Phys. Rev. B **102**, 165153 (2020).

[34] Y. Zhang, K. Deng, X. Zhang, M. Wang, Y. Wang, C. Liu, J. W. Mei, S. Kumar, E. F. Schwier, and K. Shimada, In-plane antiferromagnetic moments and magnetic polaron in the axion topological insulator candidate $EuIn_2As_2$, Phys. Rev. B **101**, 205126 (2020).

[35] J. Yan, Z. Z. Jiang, R. C. Xiao, W. Lu, W. Song, X. Zhu, X. Luo, Y. Sun, and M. Yamashita, Field-induced topological Hall effect in antiferromagnetic axion insulator candidate $EuIn_2As_2$, Phys. Rev. Res. **4**, 013163 (2022).

[36] A. B. Sarkar, S. Mardanya, S.-M. Huang, B. Ghosh, C. Y. Huang, H. Lin, A. Bansil, T. R. Chang, A. Agarwal, and B. Singh, Magnetically tunable Dirac and Weyl fermions in the Zintl materials family, Phys. Rev. Mater. **6**, 044204 (2022).

[37] C. Pei, T. Ying, Y. Zhao, L. Gao, W. Cao, C. Li, H. Hosono, and Y. Qi, Pressure-induced reemergence of superconductivity in $BaIr_2Ge_7$ and $Ba_3Ir_4Ge_{16}$ with cage structures, Matter Radiat. Extremes **7**, 038404 (2022).

[38] C. Pei, J. Zhang, Q. Wang, Y. Zhao, L. Gao, C. Gong, S. Tian, R. Luo, M. Li, and W. Yang, Pressure-induced superconductivity at 32 K in MoB_2, Natl. Sci. Rev. **10**, nwad034 (2023).

[39] C. Pei, T. Ying, Q. Zhang, X. Wu, T. Yu, Y. Zhao, L. Gao, C. Li, W. Cao, Q. Zhang, A. P. Schnyder, L. Gu, X. Chen, H. Hosono, and Y. Qi, Caging-pnictogen-induced superconductivity in skutterudites IrX_3 (X = As, P), J. Am. Chem. Soc. **144**, 6208 (2022).

[40] C. Pei, S. Jin, P. Huang, A. Vymazalova, L. Gao, Y. Zhao, W. Cao, C. Li, P. Nemes Incze, and Y. Chen, Pressure-induced superconductivity and structure phase transition in Pt_2HgSe_3, npj Quantum Mater. **6**, 98 (2021).

[41] H. Mao, J. A. Xu, and P. Bell, Calibration of the ruby pressure gauge to 800 kbar under quasi-hydrostatic conditions, J. Geophys. Res. Solid Earth **91**, 4673 (1986).

[42] A. Hammersley, S. Svensson, M. Hanfland, A. Fitch, and D. Hausermann, Two-dimensional detector software: From real detector to idealised image or two-theta scan, Int. J. High Pressure Res. **14**, 235 (1996).

[43] A. C. Larson and R. B. Von Dreele, *General Structure Analysis System (GSAS)*, Report No. LAUR 86-748 (Los Alamos National Laboratory, Los Alamos, NM, 2004).

[44] B. H. Toby, EXPGUI, a graphical user interface for GSAS, J. Appl. Crystallogr. **34**, 210 (2001).

[45] M. O. Ogunbunmi, S. Baranets, A. B. Childs, and S. Bobev, The Zintl phases AIn_2As_2(A = Ca, Sr, Ba): New topological insulators and thermoelectric material candidates, Dalton Trans. **50**, 9173 (2021).

[46] N. Guechi, A. Bouhemadou, A. Guechi, M. Reffas, L. Louail, A. Bourzami, M. Chegaar, and S. Bin Omran, First-principles prediction of the structural, elastic, electronic and optical properties of the Zintl phases MIn_2P_2 (M = Ca, Sr), J. Alloys Compd. **577**, 587 (2013).

[47] Z. Wang, G. Wang, X. Shi, D. Wang, and X. Tian, Topological phase transition in layered XIn_2P_2 (X = Ca, Sr), J. Phys. D: Appl. Phys. **50**, 465304 (2017).

[48] H. Wang, X. Zhu, Z. Chen, F. Lu, H. Li, Y. Han, L. Li, W. Gao, W. Ning, and M. Tian, Weak localization and electron-phonon interaction in layered Zintl phase $SrIn_2P_2$ single crystal, J. Phys.: Condens. Matter **33**, 245701 (2021).

[49] W.-T. Guo, Z. Huang, and J. M. Zhang, The Zintl phase compounds $AEIn_2As_2$(AE = Ca, Sr, Ba): Topological phase transition under pressure, Phys. Chem. Chem. Phys. **24**, 17337 (2022).

[50] See Supplemental Material at http://link.aps.org/supplemental/10.1103/PhysRevB.108.224510 for electronic transport of $SrIn_2As_2$ measured in atmospheric pressure and high pressure, TEM, and high-pressure XRD performed for $SrIn_2As_2$.

[51] E. Emmanouilidou, B. Shen, X. Deng, T. R. Chang, A. Shi, G. Kotliar, S. Y. Xu, and N. Ni, Magnetotransport properties of the single-crystalline nodal-line semimetal candidates $CaTX$ (T = Ag, Cd; X = As, Ge), Phys. Rev. B **95**, 245113 (2017).

[52] Y. Qi, W. Shi, P. Werner, P. G. Naumov, W. Schnelle, L. Wang, K. G. Rana, S. Parkin, S. A. Medvedev, and B. Yan, Pressure-induced superconductivity and topological quantum phase transitions in a quasi-one-dimensional topological insulator: Bi_4I_4, npj Quantum Mater. **3**, 4 (2018).

[53] C. Pei, Y. Xia, J. Wu, Y. Zhao, L. Gao, T. Ying, B. Gao, N. Li, W. Yang, and D. Zhang, Pressure-induced topological and structural phase transitions in an antiferromagnetic topological insulator, Chin. Phys. Lett. **37**, 066401 (2020).

[54] W. Cao, N. Zhao, C. Pei, Q. Wang, Q. Zhang, T. Ying, Y. Zhao, L. Gao, C. Li, and N. Yu, Pressure-induced superconductivity in the noncentrosymmetric Weyl semimetals $LaAlX$ (X = Si, Ge), Phys. Rev. B **105**, 174502 (2022).

[55] H. Cynn, J. E. Klepeis, C. S. Yoo, and D. A. Young, Osmium has the lowest experimentally determined compressibility, Phys. Rev. Lett. **88**, 135701 (2002).

[56] Y. Zhao, J. Hou, Y. Fu, C. Pei, J. Sun, Q. Wang, L. Gao, W. Cao, C. Li, and S. Zhu, Pressure-induced superconductivity in PdTeI with quasi-one-dimensional PdTe chains, Crystals **12**, 1833 (2022).

[57] K. Zhang, M. Xu, N. Li, M. Xu, Q. Zhang, E. Greenberg, V. B. Prakapenka, Y.-S. Chen, M. Wuttig, and H.-K. Mao, Superconducting phase induced by a local structure transition in amorphous Sb_2Se_3 under high pressure, Phys. Rev. Lett. **127**, 127002 (2021).

[58] Q. Wang, X.-L. Qiu, C. Pei, B.-C. Gong, L. Gao, Y. Zhao, W. Cao, C. Li, S. Zhu, and M. Zhang, Superconductivity emerging from a pressurized van der Waals kagome material $Pd_3P_2S_8$, New J. Phys. **25**, 043001 (2023).

[59] W. Li, J. Feng, X. Zhang, C. Li, H. Dong, W. Deng, J. Liu, H. Tian, J. Chen, and S. Jiang, Metallization and Superconductivity in the van der Waals compound CuP_2Se through pressure-tuning of the interlayer coupling, J. Am. Chem. Soc. **143**, 20343 (2021).

[60] Q.-G. Mu, D. Nenno, Y.-P. Qi, F.-R. Fan, C. Pei, M. ElGhazali, J. Gooth, C. Felser, P. Narang, and S. Medvedev, Suppression of axionic charge density wave and onset of superconductivity in the chiral Weyl semimetal Ta_2Se_8I, Phys. Rev. Mater. **5**, 084201 (2021).

[61] C. Pei, W. Shi, Y. Zhao, L. Gao, J. Gao, Y. Li, H. Zhu, Q. Zhang, N. Yu, C. Li, W. Cao, S. A. Medvedev, C. Felser, B. Yan, Z. Liu, Y. Chen, Z. Wang, and Y. Qi, Pressure-induced a partial disorder and superconductivity in quasi-one-dimensional Weyl semimetal $(NbSe_4)_2I$, Mater. Today Phys. **21**, 100509 (2021).

[62] L. Jennings and C. Swenson, Effects of pressure on the superconducting transition temperatures of Sn, In, Ta, Tl, and Hg, Phys. Rev. **112**, 31 (1958).

[63] A. L. Chen, S. P. Lewis, Z. Su, Y. Y. Peter, and M. L. Cohen, Superconductivity in arsenic at high pressures, Phys. Rev. B **46**, 5523 (1992).

[64] S. Mizobata, T. Matsuoka, and K. Shimizu, Pressure dependence of the superconductivity in strontium, J. Phys. Soc. Jpn. **76**, 23 (2007).

[65] K. Dunn and F. Bundy, Pressure-induced superconductivity in strontium and barium, Phys. Rev. B **25**, 194 (1982).